PAPER

Efficient orange and red thermally activated delayed fluorescence materials based on 1,8-naphthalimide derivatives†

Meiling Chen,‡[ab] Yuzhuo Chen,‡[cd] Yan Li,‡[ae] Yuhong Lin*[c] and Yunan Wu ![ORCID] *[f]

Thermally activated delayed fluorescence (TADF) molecules have emerged as a promising class of third-generation organic light-emitting diode (OLED) emitters that can achieve 100% internal quantum efficiency without the use of noble metals. However, the design of high-efficiency red TADF materials has been challenging due to limitations imposed by the energy-gap law. To overcome this challenge, two new TADF emitters, namely, 6-(4-(diphenylamino)phenyl)-2-phenyl-1*H*-benzo[*de*]isoquinoline-1,3(2*H*)-dione (**NI-TPA**) and 6-(10*H*-phenothiazin-10-yl)-2-phenyl-1*H*-benzo[*de*]-isoquinoline-1,3(2*H*)-dione (**NI-Pz**), have been synthesized and characterized. These compounds exhibit strong TADF characteristics with a small energy gap (ΔE_{ST}) between the lowest excited singlet and triplet states, short delayed fluorescence lifetimes, high thermal stability, and high photoluminescence quantum yields. The OLED devices fabricated using **NI-TPA** and **NI-Pz** as emitters show orange and red electroluminescence with emission peaks at 593 nm and 665 nm, respectively, and maximum external quantum efficiencies (EQEs) of 11.3% and 7.6%, respectively. Furthermore, applying **NI-TPA** to cell imaging yielded excellent imaging results, indicating the potential of red TADF materials in the field of biological imaging.

Introduction

Since the first organic light emitting device (OLED) was produced in 1987,[1] organic light emitting materials have played an increasingly important role in flexible displays and surface light sources.[2–6] Based on the spin-statistics theorem, molecules in organic light-emitting materials produce a 1 : 3 ratio of single to triplet excitons under electrical excitation.[7–9] To achieve highly efficient OLED light-emitting materials, it is necessary to use both single and triplet excitons simultaneously. However, in conventional OLEDs, triplet excitons are typically non-emissive,

limiting the theoretical internal quantum efficiency (IQE) of OLEDs to a maximum of 25%. Noble metal phosphorescent emitters, such as iridium and platinum complexes, can induce spin–orbit coupling (SOC) to obtain phosphorescence emission and utilize both singlet and triplet excitons.[10–12] However, their high price limits their widespread use. Therefore, the synthesis of pure organic light-emitting materials capable of utilizing both the singlet and triplet states is of great importance. In 2012, Adachi *et al.*[8] designed and synthesized the TADF material 2,4,5,6-tetra-(9-carbazolyl)-isophthalonitrile, and used it as the light-emitting layer to produce OLED devices with an external quantum efficiency (EQE) of 19.3%. This greatly exceeded the maximum EQE limit of 5% for conventional fluorescent devices. In TADF materials, triplet excitons can be transferred to singlet excitons through a reverse intersystem crossing (RISC) process to complete the radioluminescence, and both singlet and triplet excitons can be utilized to achieve efficient luminescence, with quantum efficiencies of up to 100%. Since then, much progress has been made to create highly efficient OLEDs based on TADF materials.[13–20] However, the development of orange-red TADF materials still remains a big challenge. Red TADF emitters suffer from non-radiative transitions and a quenching emission due to the low energy gap between the highest occupied molecular orbital (HOMO) and the lowest unoccupied molecular orbital (LUMO) orbitals.[21–23] Additionally, most red TADF emitters suffer from aggregation caused quenching (ACQ) effect in the solid state, leading to a decrease in their emission.[24,25]

[a] State Key Laboratory of Oncology in South China, Guangdong Provincial Clinical Research Center for Cancer, Sun Yat-sen University Cancer Center, Guangzhou 510060, China

[b] Department of Nuclear Medicine, Sun Yat-sen University Cancer Center, Guangzhou 510060, China. E-mail: chenmeil2@sysucc.org.cn

[c] Department of Ultrasound, The Fifth Affiliated Hospital, Sun Yat-sen University, Zhuhai 519000, China. E-mail: linyh97@mail.sysu.edu.cn

[d] Department of Interventional Medicine, Guangdong Provincial Key Laboratory of Biomedical Imaging, The Fifth Affiliated Hospital, Sun Yat-sen University, Zhuhai 519000, China. E-mail: chenyzh223@mail.sysu.edu.cn

[e] Department of Pathology, Sun Yat-sen University Cancer Center, Guangzhou 510060, P. R. China. E-mail: liyan1@sysucc.org.cn

[f] School of Chemistry, Sun Yat-sen University, Guangzhou 510275, China. E-mail: wuyunan@mail3.sysu.edu.cn

‡ Co-first authors.

Various efforts have been made towards achieving efficient red thermally activated delayed fluorescence (TADF) emitters, with the main approach being the development of strong electron acceptors.[26–28] The aromatic-imide group, with its rigid π-conjugated structures and strong electron-withdrawing ability, has been widely used in the construction of organic semiconductors.[29–31] 1,8-Naphthalimide (NI) group, possessing high electron affinity and two carbonyl units, has been extensively studied for its excellent hole-blocking and electron-transporting abilities.[32–35] Recently, 1,8-naphthalimide derivatives have been synthesized as efficient TADF emitters,[36–38] but there have been few reports on red TADF emitters based on NI derivatives with aggregation-induced emission (AIE) properties.

In this study, two new NI derivatives, namely **NI-TPA** and **NI-Pz**, were designed and synthesized based on a donor–acceptor (D–A) molecular architecture. These derivatives feature 1,8-naphthalimide as the electron acceptor moiety and different electron donor units of triphenylamine (TPA) or 10H-phenothiazine (Pz). Both molecules exhibited a large angle between the NI moiety and the donor, resulting in a twisted structure that facilitates efficient separation between the HOMO and LUMO. This efficient separation leads to a small energy gap (ΔE_{ST}) between the lowest singlet excited (S_1) and lowest triplet excited (T_1) states, allowing for efficient RISC and conversion of triplet excitons to singlet ones, leading to strong TADF emission. The newly developed NI materials, **NI-TPA** and **NI-Pz**, exhibit characteristic TADF properties, along with orange (551 nm) or red (645 nm) emission and high photoluminescence quantum yields (PLQYs) of up to 58% and 36%, respectively. Compared to other visible lights, red light has stronger penetration, enabling deeper biological imaging and therapy. Red light materials have lower excitation energy, which can reduce the damage of excitation light to biological tissues; and with less background interference from red light, it can reduce interference from biological backgrounds. On the other hand, TADF (Thermally Activated Delayed Fluorescence) materials generally have a longer lifespan, allowing for time-resolved imaging to reduce interference. Therefore, red light materials with TADF characteristics have unique advantages in biological imaging. We attempted to use **NI-Pz**, a red light material with TADF properties, for cell imaging.

Results and discussion

The two new NI derivatives, **NI-TPA** and **NI-Pz** (Fig. 1a), were synthesized *via* Suzuki coupling reaction and the Buchwald–Hartwig C–N coupling reaction (Scheme 1). The chemical structures of the compounds were thoroughly characterized using ^{1}H NMR, ^{13}C NMR, and high-resolution mass spectrometry (Fig. S1–S6†). The structures of **NI-TPA** and **NI-Pz** were confirmed through single-crystal X-ray diffraction analysis. As showed in Fig. 1b, the crystal structures revealed highly twisted conformations with large dihedral angles (50° for **NI-TPA**; 80° for **NI-Pz**) between the donor TPA or Pz and acceptor NI. These highly distorted geometries are believed to contribute to the effective separation of HOMO and LUMO and the occurrence of delayed fluorescence. The conformations of the crystals were
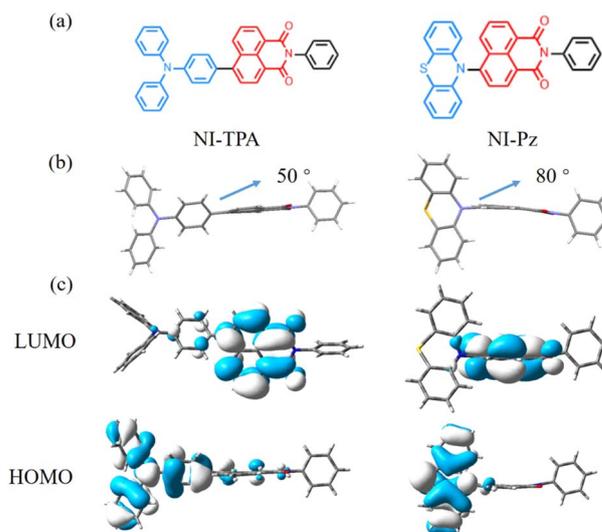

Fig. 1 (a) Molecular structures of NI compounds. (b) Crystal structures of **NI-TPA** (CCDC 2253749) and **NI-Pz** (CCDC 2253750). (c) The HOMO and LUMO orbital distributions of **NI-TPA** and **NI-Pz** based on TD-DFT at the B3LYP functional and 6-31G(d) basis.

further analysed *via* time-dependent DFT (TD-DFT) calculations to investigate the molecular orbitals and ΔE_{ST}. The HOMO and LUMO distributions of **NI-TPA** and **NI-Pz**, as presented in Fig. 1c, exhibit distinct energy levels, with the HOMO localized on the donor groups (TPA or Pz) and the LUMO distributed across the NI acceptor unit. As a result, there is small overlap between the HOMO and LUMO orbitals, resulting in small ΔE_{ST} values of 0.28 eV and 0.037 eV for **NI-TPA** and **NI-Pz**, respectively. These small ΔE_{ST} values are important for efficient RISC and the production of TADF emission. The computed HOMO/LUMO values for **NI-TPA** and **NI-Pz** were found to be −5.48/−2.63 eV and −5.54/−2.92 eV, respectively. These theoretical results are consistent with the experimental values obtained from cyclic voltammetry (CV) and absorption spectroscopy (Fig. S11,† 2a and b), which yielded HOMO/LUMO values of −5.36/−2.68 eV and −5.55/−3.03 eV, respectively.

A detailed investigation was conducted on the photophysical characteristics of **NI-TPA** and **NI-Pz**, which encompassed UV-Vis absorption, fluorescence, and phosphorescence. The UV-Vis
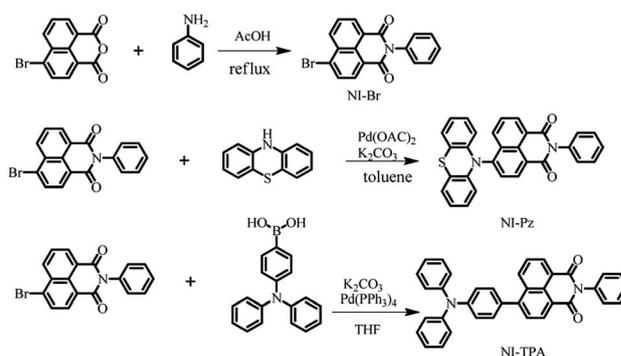
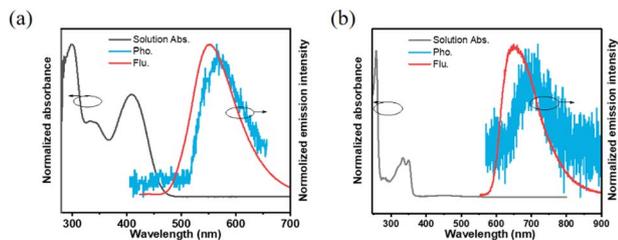Scheme 1   Synthetic route of compounds.

Fig. 2 Normalized solution absorption in tetrahydrofuran (solution abs. $c = 10^{-5}$ M), fluorescence (flu., solid state) and phosphorescence (pho., solid state at 77 K) spectra of (a) **NI-TPA** (excitation wavelength: 400 nm); (b) **NI-Pz** (excitation wavelength: 500 nm).

Fig. 4 (a) Fluorescence spectra of **NI-Pz** in THF/water mixtures ($c = 10^{-5}$ M) with different water fractions; (b) the relative fluorescence emission peak intensity of **NI-Pz** in THF/water mixtures with different water fractions.

absorption spectra in tetrahydrofuran (THF) solution (Fig. 2a and b) of both NI compounds reveal similar, intense absorption bands in the 300–350 nm range, which may be ascribed to the local excited (LE) state π–π^* transition. **NI-TPA** demonstrated strong absorption in the range of 350–450 nm, whereas **NI-Pz** exhibited weak absorption in the range of 400–500 nm, both of which were attributed to the ICT transition. Molecules with D–A structures in their excited states typically possess relatively large dipole moments, making them susceptible to solvent polarization. Therefore, they may emit distinct light signals in solvents of varying polarities, showing a tendency for increased emission wavelength with greater solvent polarity. The photophysical properties of **NI-TPA** in solvents with different polarities ($c = 10^{-5}$ M) were examined, and its UV-Vis absorption and fluorescence spectra were obtained for n-hexane (nH), toluene (tol), dioxane (Dio), tetrahydrofuran (THF), and dichloromethane (DCM). As demonstrated in Fig. 3, the UV-Vis absorption spectra of **NI-TPA** in the various solvents were comparatively similar. The fluorescence spectra exhibited a redshift with increasing solvent polarity, indicating an increase in the dipole moment of the molecule's excited state with increasing solvent polarity, and thereby confirming that the molecule's emission is caused by the intramolecular charge transition. In contrast to **NI-TPA**, the solution of **NI-Pz** exhibited relatively weak luminescence, while its solid-state powder displayed enhanced luminescence, indicative of the aggregation-induced emission (AIE) phenomenon. A series of mixed solutions with varying water content were prepared by adding water to the tetrahydrofuran solution of **NI-Pz** at different ratios. The luminescence spectra of the mixed solutions were acquired using a fluorescence

spectrometer, as illustrated in Fig. 4. The mixed solutions with lower water content exhibited negligible luminescence, while the luminescence of the mixture increased significantly upon increasing the water content up to a certain threshold. In dilute solutions, molecular freedom led to pronounced molecular vibrations, which dissipated the energy of excited-state molecules and hence resulted in luminescence quenching. However, in the solid state, molecular packing was more compact and the molecular vibration was limited, thereby reducing non-radiative transition pathways and minimizing energy loss of excited-state molecules, leading to enhanced luminescence.

The emission lifetime of the NI derivatives was investigated, revealing additional long-lived emission components in their fluorescence intensity decay curves in the solid state, as depicted in Fig. 5. Notably, the excited-state lifetime of **NI-TPA** was measured to be 9.65 μs at 300 K, while that of **NI-Pz** was slightly shorter at 55.3 μs. Furthermore, the long-lived component in the fluorescence intensity decay curves of these NI materials was found to increase gradually with rising temperature, as summarized in Table S3.† The presence of thermally activated delayed fluorescence (TADF) in these materials was confirmed by these results. The ΔE_{ST} values of the solid state were determined from the onset wavelengths of fluorescence and phosphorescence spectra (Fig. 2a and b), and were calculated to be 0.11 and 0.12 eV for **NI-TPA** and **NI-Pz**, respectively (Table S4†). These small ΔE_{ST} values facilitated efficient RISC processes, favouring highly emissive TADF in the solid state.
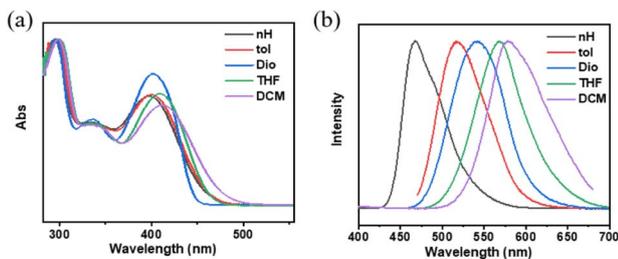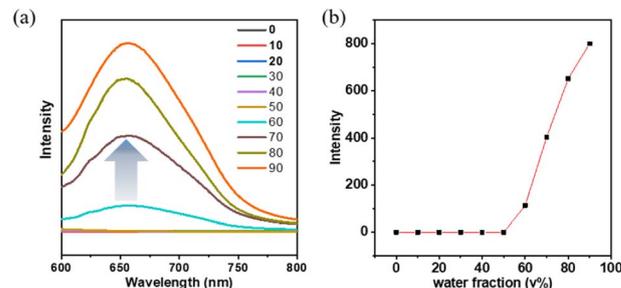

Fig. 3 (a) Normalized solution absorption ($c = 10^{-5}$ M) and (b) normalized solution fluorescence ($c = 10^{-5}$ M, excitation wavelength: 400 nm) of **NI-TPA** in different solvents.
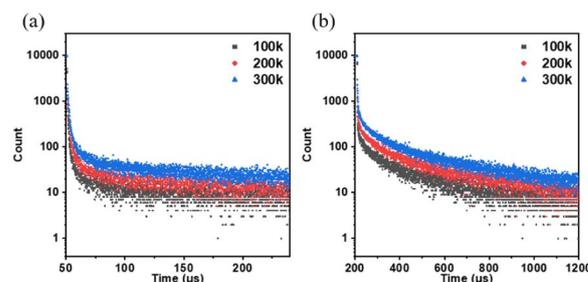

Fig. 5 Fluorescence intensity decay curve of the solid state of (a) **NI-TPA** and (b) **NI-Pz** at different temperatures.
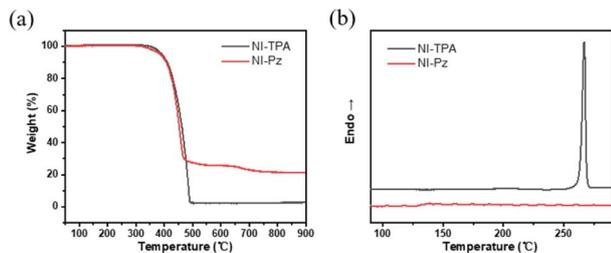
Fig. 6 (a) Thermal gravimetric analysis and (b) differential scanning calorimetry curves of **NI-TPA** and **NI-Pz**.

The thermal stability of **NI-TPA** and **NI-Pz** compounds was investigated by means of TGA and DSC analyses, as depicted in Fig. 6. It was found that both compounds exhibited exceptional thermal stability, with decomposition temperatures (T_d, 5% weight loss) as high as 391 °C for **NI-TPA** and a sublimation from 383 °C for **NI-Pz**, owing to the presence of the thermally stable imide group. The melting temperature of **NI-TPA** was determined to be 266 °C, and its high crystallinity prevented the observation of any glass transition temperature. Conversely, **NI-Pz** displayed a glass transition temperature of 138 °C and a melting temperature of 242 °C. Consequently, these compounds may provide a stable emissive layer, enhancing the lifetime of devices in practical applications. The high T_d and T_m values render **NI-TPA** and **NI-Pz** suitable for thermal evaporation processes in the fabrication of OLEDs.
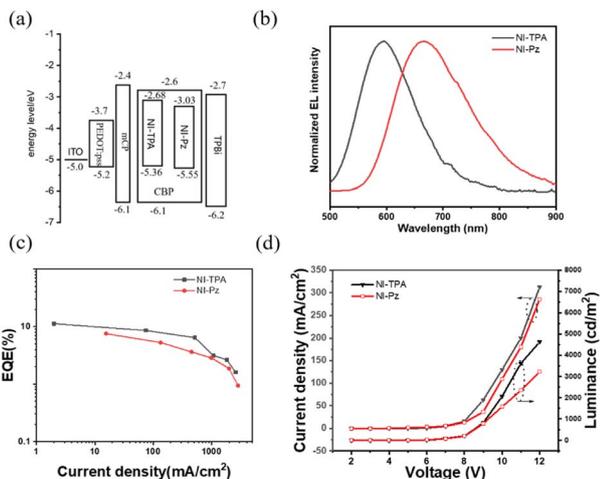

Fig. 7 (a) The energy-level diagram of the multilayer devices based on NI derivatives. The characteristics of the OLEDs based on **NI-TPA** and **NI-Pz**: (b) electroluminescence (EL) spectra at 10 V; (c) EQE–current density; (d) current density–luminance–voltage.

The two newly developed imide derivatives, **NI-TPA** and **NI-Pz**, exhibit excellent TADF, highly efficient orange and red emission, and outstanding thermal stability in their neat films. These characteristics make them highly promising candidates for orange and red OLED applications. To evaluate their potential for this purpose, OLED devices were fabricated using thermal evaporation techniques, with **NI-TPA** and **NI-Pz** serving as the emitters. The device structure included an ITO/ PEDOT:PSS (40 nm)/mCP (20 nm)/CBP:TADF emitter doped films (15 nm, 12% doping)/TPBi (40 nm)/LiF (1 nm)/Al (120 nm) configuration, as shown in Fig. 7a. The PEDOT:PSS and LiF layers acted as the hole injection and electron injection layers, respectively, while the mCP and TPBi layers served as the hole transport and electron transport layers, respectively. The high doping concentration of 12% TADF emitters doped in the CBP films allowed them to act as EMLs. The energy diagram and characteristics of these OLED devices are summarized in Fig. 7 and Table 1. The **NI-TPA** device exhibited an orange EL peak at 593 nm, while the **NI-Pz** device produced a red EL emission with a peak around 665 nm (Fig. 7b). The **NI-TPA** device exhibited better performance than the **NI-Pz** device, with a higher maximum EQE of up to 11.3% compared to 7.6% for the **NI-Pz** device (Fig. 7c). These results confirmed that both NI derivatives exhibited TADF and broke the EQE limitation (5%) of conventional fluorescent materials at similar device construction. The EL luminance of the **NI-TPA** device was also higher than that of the **NI-Pz** device (Fig. 7d). Overall, these findings demonstrate the potential of **NI-TPA** and **NI-Pz** as highly efficient and stable red emitters for OLED applications.

By using a self-assembly method, **NI-TPA** was encapsulated within F127 polymer materials to form nanoparticles, which were then introduced into cells *via* endocytosis. As shown in Fig. 8, the position of HeLa cells is located under the bright field. Then, switching to the red channel, it can be observed that red fluorescence is emitted from within the cells, indicating that the particles containing **NI-TPA** can successfully enter the cells and emit light. This demonstrates the potential of **NI-TPA** for use in biological imaging.

Experimental

Materials

6-Bromobenzo[*de*]isochromene-1,3-dione, aniline, palladium acetate, potassium carbonate 10*H*-phenothiazine, and (4-(diphenylamino)-phenyl)boronic acid were purchased from Aldrich. The other reagent were purchased from Guangzhou Jincheng company. Poly(3,4-ethylenedioxythiophene)–poly(-styrenesulfonate) (PEDOT:PSS), 4,4′-bis(9-carbazole(biphenyl)) (CBP), 1,3,5-tris(1-phenyl-1*H*-benzimidazol-2-yl)benzene

Table 1 Characteristics of OLEDs based on **NI-TPA** and **NI-Pz**

Emitter	V_{on} (V)	L_{max}, (cd m^{-2})	CE/PE/EQE (cd A^{-1}/lm W^{-1}/%)	λ_{EL} (nm)	1931 CIE coordinates (x, y)
NI-TPA	6	4634	11.3	593	(0.53, 0.45)
NI-Pz	6	3221	7.6	665	(0.61, 0.36)

(TPBi), lithium fluoride (LiF), purchased from Xi'an Baolite Photoelectric Technology company. All the materials and reagent were used as received.

Instrumentation

Nuclear magnetic resonance hydrogen spectra (^{1}H NMR) and carbon spectra (^{13}C NMR) were tested on a Bruker Avance III NMR instrument using either deuterated dimethyl sulfoxide (DMSO-d$_6$) as the solvent and tetramethylsilane (TMS) as the internal standard. Low-resolution electron bombardment mass spectrometry (EI-MS) and high-resolution electron bombardment mass spectrometry (EI-HRMS) were tested on Thermo DSQ and Thermo MAT95XP mass spectrometers, respectively. Ultraviolet-visible absorption spectra (UV-Vis) were tested using a Hitachi U-3900 spectrophotometer, and photoluminescence (PL) spectra were measured using an Ocean Optics QE65 Pro spectrometer. Fluorescence lifetime and variable temperature lifetime, time-resolved spectra, and fluorescence quantum efficiency were measured on a Horiba JY FL-3 combined steady-state/transient fluorescence spectrometer equipped with a calibrated integrating sphere for testing fluorescence quantum efficiency. Thermal properties were tested in a Shimadzu TGA-50H thermogravimetric analyser at a rate of 20 °C min^{-1} and in a differential scanning calorimetry (DSC) analyser using a NETZSCH DSC 204 F1 thermal analyser at a rate of 10 °C min^{-1}. Thermal properties were tested under nitrogen. Density Functional Theory (DFT) calculations were carried out using the Gaussian 09W program using the method and basis set B3LYP/6-31G(d) and Time-Dependent Density Functional Theory (TD-DFT) based on B3LYP/6-31G(d). The cell staining experiment was conducted by incubating the cells with **NI-TPA** for 4 hours, followed by imaging using a laser scanning confocal microscope (Zeiss LSM880).

Synthesis

6-Bromo-2-phenyl-1H-benzo[de]isoquinoline-1,3-(2H)-dione (NI-Br). A mixture of 4-bromo-1,8-naphthalic anhydride (2.77 g, 10 mmol) and aniline (1.1 g, 11.8 mmol) was added to a flask and dissolved in 100 mL acetic acid. After refluxed overnight under argon, the mixture was then poured into 300 mL water and filtered. The filter residue is collected and dried with no further purification.

Fig. 8 (a) A bright field image of HeLa cells; (b) an image of HeLa cells under the red light channel.

6-(10H-Phenothiazin-10-yl)-2-phenyl-1H-benzo[de]-isoquinoline-1,3(2H)-dione (NI-Pz). A mixture of **NI-Br** (0.5 g, 1.42 mmol) and 10-H-phenothiazine (Pz, 0.42 g, 2.13 mmol) was added to a three-necked flask and dissolved in 100 mL toluene. After stirred under argon for 30 minutes, potassium carbonate was added to the three-necked flask, followed with Pd(OAc)$_2$ (0.11 g, 0.50 mmol) and (t-Bu)$_3$PHBF$_4$ (0.22 g, 0.75 mmol). After stirred at reflux under argon for 24 h, the mixture was cooled to room temperature and poured into 50 mL water. The mixture was then extracted with 180 mL methylene chloride for 3 times. The organic layer was dried with anhydrous sodium sulphate, filtered and the filtrated solution was evaporated under reduced pressure. The crude product was purified by column chromatography on silica gel with dichloromethane and normal hexane (v/v = 1/2) as eluent. After that 0.44 g orange pure **NI-Pz** were got with a yield of 66%. ^{1}H NMR (500 MHz, DMSO) δ 8.75 (d, J = 7.7 Hz, 1H), 8.57 (dd, J = 7.2, 0.8 Hz, 1H), 8.45 (dd, J = 8.5, 0.8 Hz, 1H), 8.19 (d, J = 7.7 Hz, 1H), 7.93 (dd, J = 8.4, 7.4 Hz, 1H), 7.57 (t, J = 7.5 Hz, 2H), 7.50 (t, J = 7.4 Hz, 1H), 7.43 (dd, J = 14.4, 7.3 Hz, 2H), 7.18 (dd, J = 7.4, 1.7 Hz, 2H), 6.94–6.79 (m, 4H), 6.10 (dd, J = 8.0, 1.3 Hz, 2H). ^{13}C NMR (126 MHz, DMSO) δ 163.59, 143.26, 132.21, 131.85, 130.68, 129.99, 129.54, 129.39, 129.22, 128.76, 127.97, 127.34, 124.51, 123.91, 123.77, 119.81, 116.25. HRMS, m/z: [M]$^+$ calcd for C$_{30}$H$_{18}$N$_2$O$_2$S$_2$, 470.1089; found, 470.1080.

6-(4-(Diphenylamino)phenyl)-2-phenyl-1H-benzo[de]iso-quinoline-1,3(2H)-dione (NI-TPA). A mixture of **NI-Br** (0.5 g, 1.42 mmol) and (4-(diphenylamino)-phenyl)boronic acid (0.61 g, 2.13 mmol) was added into a flask, and dissolved with 100 mL tetrahydrofuran. After stirred under argon for 30 minutes, 1.5 g potassium carbonate dissolved in 3 mL water were added into the flask, followed with 0.02 g Pd(Ph$_3$)$_4$. The mixture was then stirred at reflux under argon for 6 hours. After cooled to room temperature, the mixture was poured to 50 mL water and extracted with methylene chloride for 3 times. The organic layer was dried with anhydrous sodium sulphate, filtered and the filtrated solution was evaporated under reduced pressure. The crude product was purified by column chromatography on silica gel with dichloromethane and normal hexane (v/v = 1/2) as eluent. After that 0.67 g orange pure **NI-TPA** were got with a yield of 92%. ^{1}H NMR (500 MHz, DMSO) δ 8.55 (t, J = 7.4 Hz, 2H), 8.46 (d, J = 8.5 Hz, 1H), 7.92 (dd, J = 8.4, 7.4 Hz, 1H), 7.85 (d, J = 7.6 Hz, 1H), 7.54 (dd, J = 15.4, 7.9 Hz, 4H), 7.47 (dd, J = 16.9, 9.5 Hz, 1H), 7.43–7.35 (m, 6H), 7.21–7.09 (m, 8H). ^{13}C NMR (126 MHz, DMSO) δ 164.20, 163.97, 148.23, 147.26, 146.39, 136.49, 132.96, 131.90, 131.50, 131.25, 130.94, 130.24, 129.86, 129.58, 129.33, 129.09, 128.67, 128.28, 127.87, 125.24, 124.28, 123.50, 122.47, 121.84. HRMS, m/z: [M]$^+$ calcd for C$_{36}$H$_{24}$N$_2$O$_2$, 516.1838; found, 516.1830.

OLED device fabrication and measurements

The substrate for the OLED device was an Indium Tin Oxide (ITO) glass substrate with a square resistance of 8 Ω m^{-2}. The ITO glass was sonicated for 15 minutes using 5% Decon detergent, deionised water, acetone and isopropyl alcohol respectively in order, and then dried in an oven. The dried ITO
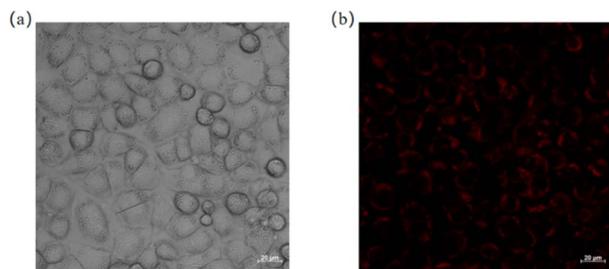
Paper

substrate was placed in an oxygen plasma cleaner for 15 min of oxygen plasma treatment. The treated ITO substrates were then placed in a spin coater and spin coated with an appropriate amount of PEDOT:PSS aqueous solution in drops at 2000 rpm for 1 min, after which the substrates were annealed at 150 °C for 20 min to remove residual moisture. The substrate was annealed at 150 °C for 20 min to remove residual moisture. The substrate covered with PEDOT:PSS was then transferred into the chamber of the vacuum vapour deposition apparatus, where the organic layer and the metal layer were vapour deposited in turn. The vacuum level of the chamber was below 4×10^{-4} Pa. The deposition rates of the organic and metal layers were 0.5–1 Å s^{-1} and 3–5 Å s^{-1} respectively. The effective luminescence area of the prepared devices was 20 mm^2. Performance testing of the OLED devices was carried out in air and the devices were not encapsulated. The voltage, current density, luminance characteristics and electroluminescence (EL) spectra were measured using a Keithley 2400 source meter in conjunction with a Photo Research 735 spectrometer. Based on this, current efficiency, power efficiency and external quantum efficiency (EQE) was further calculated. The EQE was calculated from the voltage, current, luminance and EL spectrum parameters using Matlab software.

Conclusions

In this study, two D–A type imide derivatives featuring strong electron-deficient 1,8-naphthalimide as acceptor moiety and nonplanar strong electron-rich groups, TPA and Pz, as donor groups, were synthesized and characterized for their excellent TADF properties. The twist conformations of **NI-TPA** and **NI-Pz** in the solid state effectively restricted their intermolecular motions, resulting in typical highly orange and red emissions at 551 and 645 nm, respectively, with high solid-state PLQY of 58 and 36%. Furthermore, the effective separation of their HOMO/LUMO electron distribution resulted in small ΔE_{ST} values of 0.05 and 0.13 eV for **NI-TPA** and **NI-Pz**, respectively. The small ΔE_{ST} values enabled the NI derivatives to possess excellent TADF, which was confirmed by the clear thermally activated delayed component of the fluorescence intensity decay curves. The morphological stability of the NI derivatives in a large temperature range also ensured a stable EML, which improved the lifetime of devices in practical applications. The optimized TADF OLEDs based on **NI-TPA** and **NI-Pz** exhibited maximum EQE values of 11.3% and 7.6% with EL peaks at 593 and 665 nm, respectively. These readily available 1,8-naphthalimide derivatives hold great promise for the design of highly efficient orange and red OLEDs. Additionally, **NI-TPA** shows excellent compatibility with HeLa cells and yields great imaging results, indicating the potential of red TADF materials in the field of biological imaging.

Conflicts of interest

There are no conflicts to declare.

References

1 C. W. Tang and S. A. VanSlyke, *Appl. Phys. Lett.*, 1987, **51**, 913–915.
2 Z. Yang, Z. Mao, Z. Xie, Y. Zhang, S. Liu, J. Zhao, J. Xu, Z. Chi and M. P. Aldred, *Chem. Soc. Rev.*, 2017, **46**, 915–1016.
3 C. Wang, S. Wang, W. Chen, Z. Zhang, H. Zhang and Y. Wang, *RSC Adv.*, 2016, **6**, 19308–19313.
4 T.-W. Ha, Y.-B. Kim, G.-S. Heo, I. Hwang, H. G. Jeon and B. Park, *RSC Adv.*, 2016, **6**, 33063–33071.
5 M. S. Weaver, M. A. Fusella, R. Saramak, R. Bushati, H. Mundoor, V. M. Menon, N. J. Thompson and J. J. Brown, *J. Mater. Chem. C*, 2022, **10**, 4182–4186.
6 A. Nyga, T. Kaihara, T. Hosono, M. Sipala, P. Stachelek, N. Tohnai, S. Minakata, L. E. de Sousa, P. de Silva, P. Data and Y. Takeda, *Chem. Commun.*, 2022, **58**, 5889–5892.
7 A. Endo, M. Ogasawara, A. Takahashi, D. Yokoyama, Y. Kato and C. Adachi, *Adv. Mater.*, 2009, **21**, 4802–4806.
8 H. Uoyama, K. Goushi, K. Shizu, H. Nomura and C. Adachi, *Nature*, 2012, **492**, 234–238.
9 K. Kimura, K. Miwa, H. Imada, M. Imai-Imada, S. Kawahara, J. Takeya, M. Kawai, M. Galperin and Y. Kim, *Nature*, 2019, **570**, 210–213.
10 B. Minaev, G. Baryshnikov and H. Agren, *Phys. Chem. Chem. Phys.*, 2014, **16**, 1719–1758.
11 S. Yoon and T. S. Teets, *Chem. Commun.*, 2021, **57**, 1975–1988.
12 M. Savitha Lakshmi and S. Mahalakshmi, *Mol. Syst. Des. Eng.*, 2022, **7**, 1172–1206.
13 P. L. Santos, J. S. Ward, P. Data, A. S. Batsanov, M. R. Bryce, F. B. Dias and A. P. Monkman, *J. Mater. Chem. C*, 2016, **4**, 3815–3824.
14 H. M. Kim, J. M. Choi and J. Y. Lee, *RSC Adv.*, 2016, **6**, 64133–64139.
15 Y. Xiang, Y. Zhao, N. Xu, S. Gong, F. Ni, K. Wu, J. Luo, G. Xie, Z.-H. Lu and C. Yang, *J. Mater. Chem. C*, 2017, **5**, 12204–12210.
16 X. Zhou, M. Huang, X. Zeng, T. Chen, G. Xie, X. Yin and C. Yang, *Polym. Chem.*, 2019, **10**, 4201–4208.
17 Q. T. Siddiqui, A. A. Awasthi, P. Bhui, P. Parab, M. Muneer, S. Bose and N. Agarwal, *RSC Adv.*, 2019, **9**, 40248–40254.
18 J. G. Yu, S. H. Han, H. L. Lee, W. P. Hong and J. Y. Lee, *J. Mater. Chem. C*, 2019, **7**, 2919–2926.
19 J. Liang, C. Li, Y. Cui, Z. Li, J. Wang and Y. Wang, *J. Mater. Chem. C*, 2020, **8**, 1614–1622.
20 N. N. T. Nguyen, H. Mubarok, T. Lee, T. Q. Tran, J. Jung and M. H. Lee, *RSC Adv.*, 2022, **12**, 29892–29899.
21 W. Qin, D. Ding, J. Liu, W. Z. Yuan, Y. Hu, B. Liu and B. Z. Tang, *Adv. Funct. Mater.*, 2012, **22**, 771–779.
22 G. Qian, Z. Zhong, M. Luo, D. Yu, Z. Zhang, Z. Y. Wang and D. Ma, *Adv. Mater.*, 2009, **21**, 111–116.

23 H. Lu, Y. Zheng, X. Zhao, L. Wang, S. Ma, X. Han, B. Xu, W. Tian and H. Gao, *Angew Chem. Int. Ed. Engl.*, 2016, **55**, 155–159.

24 T. M. Figueira-Duarte, P. G. Del Rosso, R. Trattnig, S. Sax, E. J. List and K. Mullen, *Adv. Mater.*, 2010, **22**, 990–993.

25 L. Wang, Z. Zheng, Z. Yu, J. Zheng, M. Fang, J. Wu, Y. Tian and H. Zhou, *J. Mater. Chem. C*, 2013, **1**, 6952–6959.

26 L. Yu, Z. Wu, G. Xie, W. Zeng, D. Ma and C. Yang, *Chem. Sci.*, 2018, **9**, 1385–1391.

27 H. Liu, K. Zhang, H. Zou, Q. Mu, Y. Song, L. Lin, Y. Xu, C. K. Wang and J. Fan, *Phys. Chem. Chem. Phys.*, 2023, **25**, 1032–1044.

28 H. Wang, J. Wang, P. Zou, J. Xu, J. Li, H. Shi, Z. Zhao and B. Z. Tang, *Mater. Chem. Front.*, 2023, **7**, 1633–1641.

29 H. Sun, L. Wang, Y. Wang and X. Guo, *Chemistry*, 2019, **25**, 87–105.

30 Q.-H. Ling, J.-L. Zhu, Y. Qin and L. Xu, *Mater. Chem. Front.*, 2020, **4**, 3176–3189.

31 C. Li, Z. Lin, Y. Li and Z. Wang, *Chem. Rec.*, 2016, **16**, 873–885.

32 P. Ledwon, A. Brzeczek, S. Pluczyk, T. Jarosz, W. Kuznik, K. Walczak and M. Lapkowski, *Electrochim. Acta*, 2014, **128**, 420–429.

33 Y. Xie, L. Du, X. Li, B. Yuan, G. Bao and L. Wang, *Dyes Pigm.*, 2022, **207**, 110691.

34 G. Sivakumar, A. H. Bertoni, H.-S. Kim, P. E. Marchezi, D. R. Bernardo, A. Hagfeldt, M. Grätzel, S. M. Zakeeruddin and A. F. Nogueira, *Synth. Met.*, 2019, **249**, 25–30.

35 T. T. Do, H. D. Pham, S. Manzhos, J. M. Bell and P. Sonar, *ACS Appl. Mater. Interfaces*, 2017, **9**, 16967–16976.

36 J. H. Yun and J. Y. Lee, *Dyes Pigm.*, 2017, **144**, 212–217.

37 H. F. Higginbotham, P. Pander, R. Rybakiewicz, M. K. Etherington, S. Maniam, M. Zagorska, A. Pron, A. P. Monkman and P. Data, *J. Mater. Chem. C*, 2018, **6**, 8219–8225.

38 N. Masimukku, D. Gudeika, D. Volyniuk, O. Bezvikonnyi, J. Simokaitiene, V. Matulis, D. Lyakhov, V. Azovskyi and J. V. Gražulevičius, *Phys. Chem. Chem. Phys.*, 2022, **24**, 5070–5082.